

A unified multiscale 3D printer combining single-photon Tomographic Volumetric Additive Manufacturing and Two-Photon Polymerization

Buse Unlu^{1,*}, Felix Wechsler¹, Ye Pu¹, Christophe Moser¹

¹Laboratory of Applied Photonics Devices, School of Engineering, Ecole Polytechnique Fédérale de Lausanne, CH-1015, Lausanne, Switzerland

Corresponding author: buse.unlu@epfl.ch

Abstract

Photopolymerization-based additive manufacturing enables cost-effective, high-speed fabrication of complex 3D structures but is inherently constrained by a trade-off between resolution and printing speed. Single-photon polymerization ensures rapid polymerization of centimeter-scale structures with features on the order of tens of micrometers, whereas two-photon polymerization provides sub-micrometer features at sub-millimeter scales. Here, we introduce a hybrid unified 3D printer that leverages the complementary strengths of both printing mechanisms to bridge this scale–resolution gap.

We propose integrating two-photon polymerization (2PP) for high-resolution, localized spatial control with single-photon Tomographic Volumetric Additive Manufacturing (TVAM) for enabling rapid, high-throughput 3D fabrication. In this approach, TVAM first forms millimeter-scale volumetric structures attached on a glass rod, via overprinting, which is then accessible, on the same platform, for subsequent high-resolution 2PP. Without needing to change the photoresin or introducing intermediate post-processing steps, we proceed to demonstrate finely printed structures via 2PP using a tightly focused femtosecond laser beam, fabricated both inside (embedded within) and on the surface of the millimeter-scale 3D objects printed with TVAM. Here, TVAM contributes in two distinct ways: by generating a pre-polymerized volume that facilitates subsequent 2PP, and by directly driving volumetric polymerization in designated regions within seconds. We experimentally demonstrate that this dual-mode strategy provides a scalable approach for rapidly fabricating millimeter-scale 3D structures featuring sub-micrometer details. For applications such as biomedical scaffolds and tissue engineering, tens of micrometer-scale features are sufficient across the majority of the volume, with higher resolution confined to localized functional regions. For optical component manufacturing, the distinct refractive indices of the 2PP and TVAM regions can be exploited for light propagation and other micro-optical functionalities.

1. Introduction

Light-based additive manufacturing has emerged as a powerful fabrication technique, enabling precise and flexible fabrication of complex three-dimensional (3D) designs with high speed, and broad material versatility and compatibility, which are challenging to achieve using conventional manufacturing approaches [1–3]. In particular, techniques such as tomographic volumetric additive manufacturing (TVAM) and two-photon polymerization (2PP) exemplify

these advantages, with TVAM enabling rapid, volumetric fabrication of structures [4–6] and 2PP allowing precise fabrication of intricate microscale features [7,8].

TVAM is a single-photon [4,6,9] absorption 3D-printing technique that relies on the projection of tomographic patterns onto a rotating photocurable resin container. A photoinitiator inside the resin absorbs light and triggers a photopolymerization reaction. Due to the rotation of the resin container, the absorbed light dose can be controlled in 3D via tomographic projections, and once a local dose threshold is reached, a stable polymerization network is formed [2,10], building the object. Because of its simple implementation, amplitude modulation with digital micromirror device (DMD) is commonly employed, although phase-modulated pattern projection is also possible [11]. Typical TVAM requires printing times in the range of 5 to 30 seconds and, currently, experimental prints reach up to several centimeters in extent [12], but only down to around 20 μm minimum feature size for millimeter-scale objects [13].

One of the challenges in TVAM is the computation of the tomographic patterns. As light is projected onto a cuvette filled with resin, several optical effects, such as refraction, absorption, and scattering, can occur. As optical rays propagate through the resin, the absorbed intensity needs to be stored for each voxel. These operations can be approximated by the attenuated Radon transform [4,14], but are more accurately described by a full ray-tracing model [15,16]. Wave-optical pattern simulation is possible [17], but its superiority has yet to be shown experimentally. To optimize a suitable set of patterns, Rackson et al. [18] developed an iterative optimization scheme based on the thresholding behavior of the resin, such that object regions receive a dose above an upper threshold, and void regions remain below a lower threshold. This idea can be transformed into an inverse problem in which a loss function is minimized using gradient-descent-based algorithms [17,19–21].

TVAM is flexible in that a wide range of materials and applications have been demonstrated [22], including bioprinting [6]. Because of the rotation of the vial, TVAM is especially powerful for overprinting existing elements, as demonstrated by the overprinting of a screwdriver handle in an early work [4]. Recent studies have explored more complex overprinting scenarios involving absorptive, reflective, scattering, and transparent materials [23,24], which is possible by taking the optical effects of existing structures into account.

Two-photon polymerization, in contrast to TVAM, is a nonlinear process in which a molecule absorbs two photons simultaneously. This effect is more pronounced within the focal point of a tightly focused femtosecond (fs) pulsed laser [25–27]. The printing process relies on scanning the fs laser pulses spot by spot to generate individual voxels, which are then assembled layer by layer to construct the final structure [26,28].

Although the localized confinement in the volume enables 3D micro- and nanofabrication with a high-precision, reaching below 100 nm [29,30], this capability comes at the cost of limited volumetric throughput due to the reliance on serial scanning, and the requirement for high peak intensities arising from the low two-photon absorption cross-section [25,31]. Overcoming this limitation has therefore led to development of various high-speed printing strategies, mainly through the application of advanced scanning techniques such as galvo and resonant scanners [32,33], pattern projections methods including diffraction optical elements [34] and DMD enabling multiple-foci printing [35,36], and optimized photoresin formulations [37,38]. Not only have the 2PP optical setups been improved, but 2PP has also been combined with other additive manufacturing methods, most notably single-photon polymerization (1PP) [39–42]. Illustratively, regions requiring high resolution are printed using 2PP, while the remaining parts of the device are solidified via 1PP using UV light [39,42]. Alongside these spatially separated hybrid approaches, single-photon absorption is also employed to pre-

sensitize the photoresin prior to 2PP, depleting oxygen in the resin. At the same spatial location, 2PP subsequently solidifies the pre-sensitized material with a lower required fs laser dose, achieving accelerated printing while also improving axial confinement [41].

Despite these advancements, the trade-off between high-throughput and high-resolution fidelity has been partially addressed, yet it remains insufficient for many applications. We therefore propose addressing this challenge by combining 2PP with TVAM. Due to the orthogonal illumination geometry of TVAM with respect to 2PP, their combination inherently brings more flexibility than previous attempts combining DLP/SLA and 2PP. In our experimental setup, a glass vial containing a photocurable resin is illuminated with tomographic light patterns from multiple angular directions using a 405 nm continuous-wave (CW) laser diode, while a glass rod serves as the build platform. The rod is attached to a second rotation platform which is synchronized with the rotation of the vial. When the accumulated light dose from the projected patterns exceeds the polymerization threshold of the resin, localized polymerization is initiated on top of the glass rod. Overprinting enables flexible access to the target surface for subsequent 2PP. Without removing the sample or applying post-processing, the structure is further processed by 2PP using a femtosecond (fs) pulsed laser at 780 nm. While TVAM-printed structures typically require additional UV post-curing to achieve sufficient mechanical rigidity, 2PP directly yields solid and mechanically stable microstructures [2,43]. Despite the different crosslinking characteristics of the two polymerization mechanisms, we experimentally demonstrate 3D-printed objects that exhibit micrometer-scale features, successfully achieving high-resolution definition both at the surface and within the volumetrically polymerized, millimeter-scale structures.

This hybrid printing approach is particularly attractive for applications requiring rapid fabrication of millimeter-scale structures with localized sub-micrometer features, such as bioengineered scaffolds and microfluidic devices. Moreover, the distinct refractive indices of the regions printed by 2PP and TVAM [42,44,45] can be exploited for light guiding, enabling micro-optical components such as waveguides, microlenses and other integrated photonic functionalities.

2. Materials and Methods

2.1 Experimental setup

We first constructed TVAM and 2PP setups separately (comprehensive sketches of the experimental setups are depicted in Supplementary Material Figure S1 and Figure S2, respectively) and then integrated them to form the hybrid platform shown in Figure 1. A real photograph of the printing region in the combined TVAM and 2PP setup is provided in Supplementary Material Figure S3. For the TVAM setup, a continuous-wave (CW) laser diode at 405 nm is coupled into a square-core multimode fiber that illuminates the aperture of DMD (V-7000 VIS, Vialux). The generated DMD patterns, described in Section 2.2, are demagnified by a factor of two using a pair of achromatic doublets (L1 and L2 with 300 mm and 150 mm focal lengths, respectively) and imaged into a quartz glass vial (refractive index 1.4696, inner diameter 4.30 mm) containing the photocurable resin. Ray-tracing simulations were performed to model the aberration of the beam spot in the printing region using Zemax OpticStudio, a root-mean-square (RMS) point-spread-function (PSF) diameter of 6.8 μm (see Supplementary Material Figure S4). The TVAM printing region is monitored by a camera (C1), using a pair of achromatic doublet lenses (L3, 75 mm focal length).

For 2PP, a mode-locked Ti:Sapphire femtosecond pulsed laser beam at 780 nm (repetition rate 80 MHz, pulse duration 70 fs) is directed onto a phase-only liquid crystal on silicon (LCOS) Spatial Light Modulator (SLM, PLUTO-2.1, Holoeye), which provides lateral scanning of the fs laser spot over the printing region by changing the period of a blazed grating. The beam is then focused on the tip of a glass rod (refractive index 1.4814, diameter 1 mm) that serves as a printing platform, using a 20x/0.45 numerical aperture (NA) microscope objective. The 2PP printing process is monitored via the camera (C2) through the combination of the objective lens, a long-pass dichroic mirror (cut-on wavelength at 699 nm) and a tube lens (TL, 40 mm focal length). The same imaging system is used to ensure that the fs laser beam is precisely focused onto the printing surface by monitoring its specular reflection. A detailed description of the complete 2PP system and procedure is provided in the Supplementary Materials S2 and mainly in our previous publication [41].

Both the glass vial and the glass rod are mounted on separate motorized rotary stages (X-RSW60C, Zaber) respectively, each placed on a one-axis motorized translation stage that provides z-axis motion. The two rotary stages are synchronized to rotate simultaneously via an external controller (X-MCC2, Zaber), enabling overprinting of TVAM structures onto the glass rod. To ensure time synchronization between all devices, the Zaber rotary stages serve as a clock. It provides regular synchronization signals to an Arduino Nano Every, which then forwards these signals to the VialuxDMD display. Based on rotation speed and the number of patterns, the DMD displays each pattern for a certain amount of time.

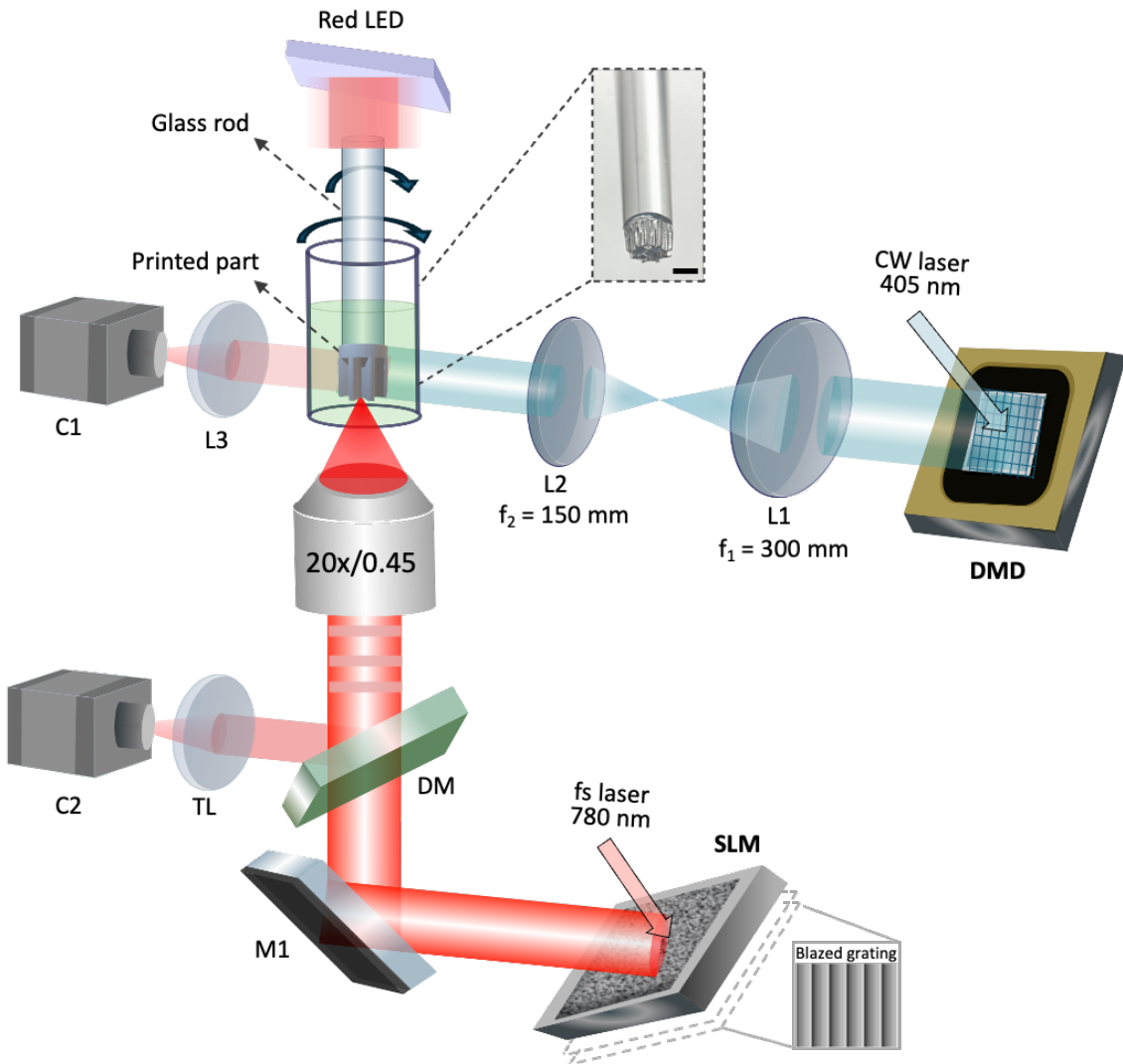


Figure 1. Schematic illustration of the experimental setup for the multiscale 3D Printer combining Single-Photon Tomographic Volumetric Manufacturing and Two-Photon Polymerization: lens, C: camera, M: mirror, DM: dichroic mirror, TL: tube lens. The inset shows a real photograph of a TVAM-overprinted gear structure on a glass rod. The scale bar is 500 μm .

2.2 Pattern optimization

In this part, we provide details about the pattern optimization process for the tomographic projections in TVAM. The patterns are calculated with the open-source software Dr.TVAM [16,23] which models ray optical effects such as refraction, absorption, and reflection. Dr.TVAM steps each DMD pixel as a geometrical ray through a discretized voxel grid. At each step, some of the carried light intensity is absorbed by the voxel according to Beer-Lambert's law, and the ray is attenuated. This procedure is repeated until the ray leaves the vial. Overall, the absorbed dose is calculated by summing the absorbed doses of each individual ray from the DMD pixels and all angles. In our case, in addition to attenuation, we also have reflection and refraction on the air-glass-resin interfaces. Further, since we overprint a portion of the structures over the glass rod, we additionally need to model that light propagating from the

resin into the glass rod. Inside the glass rod, there is no attenuation. However, there is refraction and reflection which is handled by the Dr. TVAM framework physically correctly. We are using the following loss function in our gradient-descent-based optimization

$$\mathcal{L} = w_{in} \cdot \underbrace{\sum_{v \in \text{object}} \text{ReLU}(t_u - I_v)^2}_{\text{force polymerization in object}} + w_{out} \cdot \underbrace{\sum_{v \notin \text{object}} \text{ReLU}(I_v - t_l)^2}_{\text{prevent polymerization elsewhere}} + w_o \cdot \underbrace{\sum_{v \in \text{object}} \text{ReLU}(I_v - 1)^2}_{\text{avoid over-polymerization}} + w_{sparsity} \cdot \underbrace{\sum_{j \in \text{object}} |P_j|^D}_{\text{enforce non-sparse patterns}} \quad (1)$$

In this equation, I_v represents the absorbed intensity in voxel v after the projection of the patterns. P_j denotes the value of the j -th pixel of the patterns. The variables t_u and t_l correspond to the upper and lower thresholds, respectively. The weights w_{in} , w_{out} , w_o , and $w_{sparsity}$ are relative coefficients for the respective terms. The parameter D imposes varying penalties for sparse values. The general goal of this loss function is to find a set of patterns such that projected intensity results in an absorbed dose where object voxels cross the polymerization threshold, and void voxels stay below it. In practice, a set of right printing time and printing power needs to be experimentally determined to obtain a correctly cured print. For our experiments, for a gear structure, we set $t_l = 0.7$, $t_u = 0.9$, $D = 4$, $w_{in} = w_{out} = w_o = 1$, while for two stacked rectangular prisms with lateral through-holes, we chose $w_{sparsity} = 1.0$. The sparsity term allows us to increase the pattern efficiency of our patterns, which reduces printing time and laser power. For the gear, we did not use sparsity tuning and hence $w_{sparsity} = 0$. The glass rod, on which the elements were printed, was modeled with a refractive index of $n = 1.4814$ and a diameter of 1 mm. The optimization time on an NVIDIA L40s was around 3 minutes. The full configuration files and meshes can be found at: <https://github.com/EPFL-LAPD/A-unified-multiscale-3D-printer-combining-single-photon-TVAM-and-Two-Photon-Polymerization>.

Figure 2a demonstrates the projection of optimized tomographic patterns of the prisms (inverted) onto a glass rod dipped into the resin for overprinting, where θ_i to θ_m represent examples of optimized light patterns from different angles projected by the DMD. An example of the pattern at 0° is shown in Figure 2b. The final absorbed light dose from the legs of the small prism, after projecting all tomographic patterns, is depicted in Figure 2c.

It is important to note that, although an index-matching bath is commonly used in TVAM, in our case we did not need to employ one but instead relied on refraction correction by Dr. TVAM. This simplifies the experimental procedure, particularly for 2PP, since the objective lens (OBJ) requires a coverglass thickness of 170 μm to ensure proper aberration correction and optimal focusing.

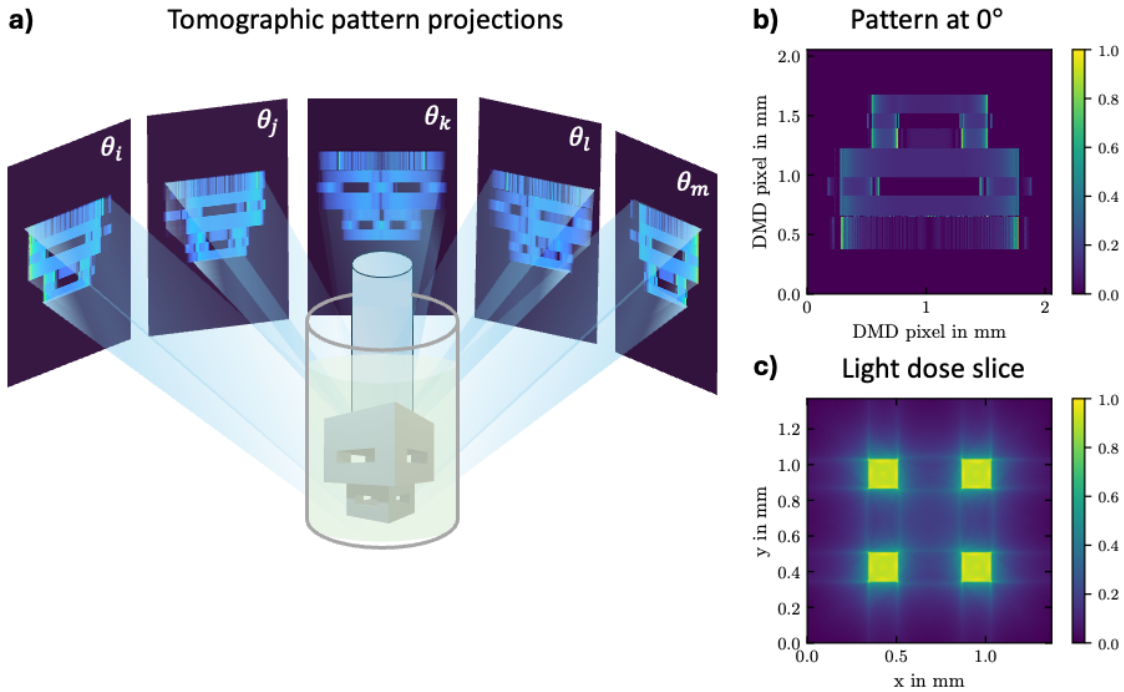


Figure 2. Pattern optimization for TVAM. a) Projection of optimized tomographic patterns (increased contrast for visibility), overprinting two stacked rectangular prisms (inverted) onto a glass rod. θ_i to θ_m represent examples of optimized light patterns projected by the DMD. b) An example pattern for the prisms at 0° and c) The final absorbed light dose after projecting all tomographic patterns, a slice taken from the 3D dose of the small prism's legs.

2.3 Materials

A photocurable resin composed of diurethane dimethacrylate (DUDMA) and poly(ethylene glycol) diacrylate (PEGDA, average Mn 700) in a 4:1 weight ratio is used for fabrication, with 1.35 wt.% ethyl-2,4,6trimethylbenzoylphenylphosphinate (TPO-L) as the photoinitiator, enabling both single- and two-photon excitation [41,46–49]. The refractive index of the resin was measured to be 1.4827 at 405 nm. The absorbance of the resin formulated with 1.35 wt.% TPO-L was calculated to be 4.695, corresponding to an extinction coefficient of 1.081 mm^{-1} , as detailed in the Supplementary Materials Figure S5, which is used in the pattern optimizations.

3. Results and discussion

We designed the gear structure shown in Figure 3a using a computer-aided design (CAD) software for printing by TVAM. The height and width of the gear were set to 1.1 mm, and the portion to be overprinted on the glass rod was 225 μm in height. For 2PP, two-dimensional (2D) image of the QR code of our group website and its letters, as shown in Figure 3b, served as patterns for scanning by the SLM. In the experiment, before placing the resin vial, the DMD light patterns of the gear structure were sent, and the position of the rod was aligned to the designed location using a motorized linear stage controlled by MATLAB software, where the alignment was verified using the camera C1 in Figure 1. Also, the location of rod where the fs laser beam is focused (working distance) was recorded for use in 2PP. The vial and glass rod were then mounted on rotary stages and positioned at the center of the DMD image plane. To ensure a uniform rotational state of the viscous resin, the glass vial was rotated for three

full turns prior to DMD illumination. This pre-rotation prevents a rotational velocity mismatch within the resin that would otherwise lead to curved gear teeth, as illustrated in Figure S6. The optimized 2D patterns described in Section 2.2 were projected onto the photocurable resin with a light dose of 45.3 mJ/cm^3 (the calculation is provided in the Supplementary Materials). Within 12 seconds, the gear was overprinted onto the glass rod. Without removing the gear-overprinted rod or applying any post-processing steps, the rod was simply moved downward using the motorized stage to reach the working distance of the objective lens (in Figure 1), thereby initiating 2PP. The hatching distance (distance between the voxels, lateral overlap) was set to 760 nm along both the x- and y-axes, while the slicing distance (distance between two consecutive layers) was 0.8 μm . We printed a two-layer QR code on the surface of the gear using an average IR fs laser power of 13 mW and an exposure time of 50 ms per laser spot. After the printing process, the final print was removed from the glass rod. Then, the residual resin surrounding the structures was rinsed in isopropanol (IPA) and post-cured under a UV lamp (Solis-405C, Thorlabs) for 1 minute. Figure 3c shows the scanning electron microscope (SEM) image of the final object, a millimeter-scale TVAM-overprinted gear featuring sub-micrometer details fabricated by 2PP. A minimum axial resolution of 270 nm was obtained, which is well below the diffraction limit of our optical system, as can be observed in the magnified inset of Figure 3c. Due to the sub-micrometer feature size, insufficient optical contrast and minor defects, the QR code cannot be decoded using a smartphone camera [50].

In a second experiment, by placing the rod off-center relative to the focus of the objective lens, the system enables more structures to be printed by 2PP at multiple locations along the rotational path of the TVAM-overprinted structure. Figure 3d illustrates the sequential 2PP-printed structures, including the QR code and letters, using the same printing parameters as in the previous experiment. The image was captured by the system camera C2 (in Figure 1) right after the printing process, before the post-processing steps.

In addition, a further experiment was conducted in which 2PP printing was performed during continuous rod rotation. Instead of scanning the fs laser beam using the SLM, the beam with 13 mW average power remained at the same location on the gear while the rod was rotated at an angular speed of $2 \text{ }^\circ/\text{s}$. Figure 3e presents the 2PP-printed structure, with an approximate diameter of 168 μm , obtained by two consecutive full rotations of the rod, enabling direct printing over an extended area on top of the gear. While the rotation of the rod is a requirement for TVAM, these experiments show that it can be advantageously adapted for 2PP, thereby increasing the accessible field-of-view (FOV) on the TVAM-printed structure, and extending the versatility and functionality of the multiscale 3D printer setup.

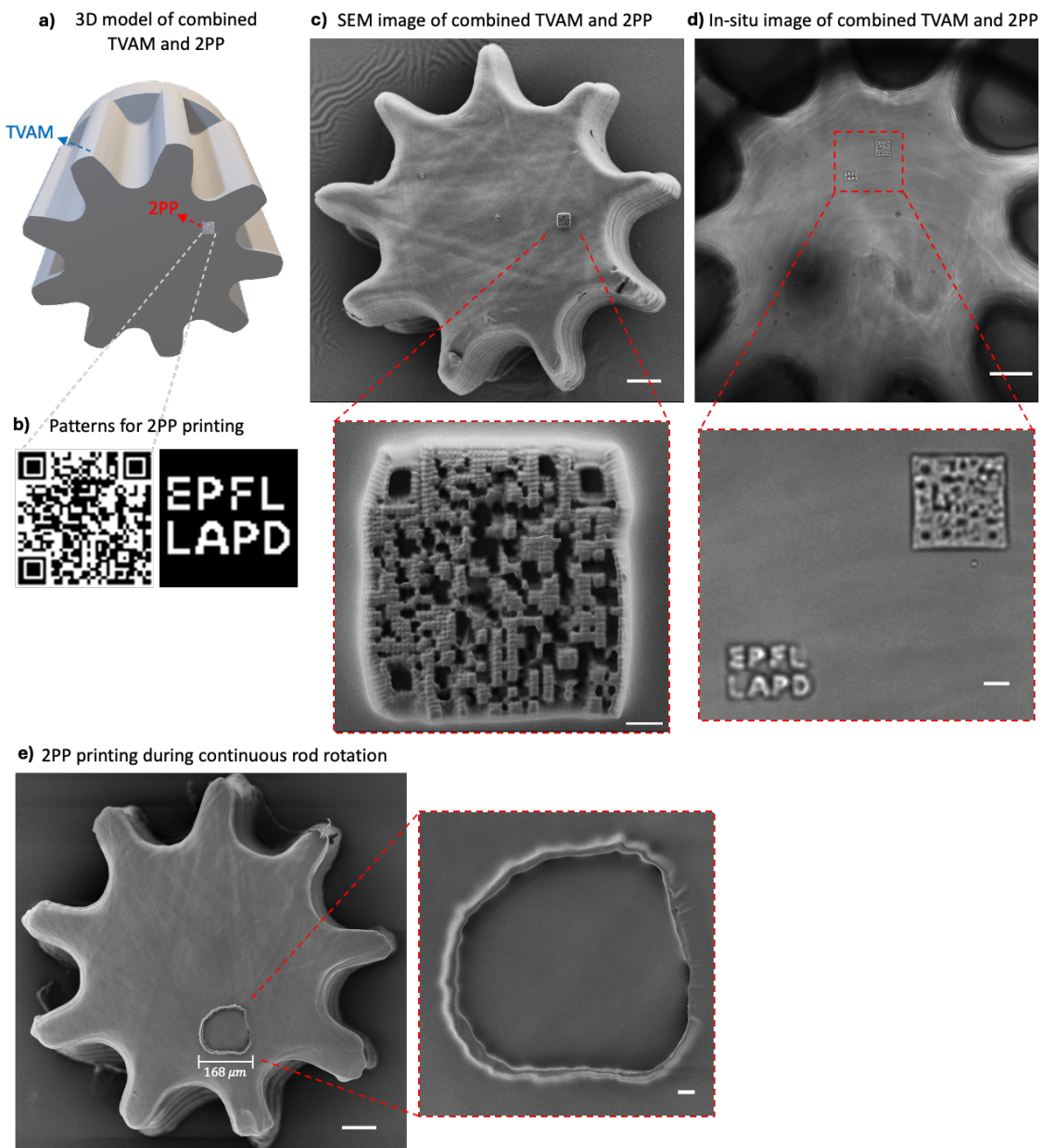


Figure 3. Millimeter-scale TVAM-overprinted gear with sub-micrometer details fabricated by 2PP. a) 3D CAD model for the combination of TVAM (gear) and 2PP (QR code) printing. b) The 2D image patterns for 2PP printing. c) SEM image of the final structure printed by a combination of TVAM and 2PP. The inset shows a magnified view of the QR code printed by 2PP. Scale bars are 100 μ m and 5 μ m, respectively. d) Camera-captured image of a gear featured by sequential 2PP-printed features (QR code and letters), formed by rotating the glass rod. The inset is a magnified view of the 2PP-printed structures. The scale bars are 100 μ m and 10 μ m, respectively. e) 2PP-printed structure (\sim 168 μ m) during the continuous rod rotation on the TVAM-printed gear. The scale bars are 100 μ m and 10 μ m, respectively.

Following the gear fabrication, a more complex 3D structure shown in Figure 4a was designed. It consists of two stacked rectangular prisms (1.1 x 1.1 x 0.85 mm and 0.68 x 0.68 x 0.45 mm) with lateral through-holes (1.1 x 0.60 x 0.15 and 0.68 x 0.36 x 0.13 mm) for printing with

TVAM, and a bridge-like structure with four legs (36 x 36 x 28 μm) and a top hole (15 x 15 x 4 μm) for 2PP. The portion of the bigger rectangular prism to be overprinted on the glass rod (inverted) was 275 μm in height.

The optimized 2D light patterns mentioned in Section 2.2 were projected onto the resin with a light dose of 51.3 mJ/cm^3 , and within 12 seconds, the structure composed of rectangular prisms was overprinted onto the glass rod. The rod was then moved downward using the motorized stage until it reached the working distance of the objective lens (in Figure 1). At this location, 2PP was initiated. The hatching distance was set to 760 nm along both the x- and y-axes, while the slicing distance was 1.2 μm . The bridge-like structure (23 layers) was printed on the surface of the smaller rectangular prism using an average IR fs laser power of 18 mW and an exposure time of 50 ms per laser spot. After printing, the final structure was removed from the glass rod, and the unsolidified resin was washed out with IPA. Figure 4b shows a digital microscope (VHX-5000, Keyence) image of the final object, which comprises TVAM and 2PP structures printed sequentially on top of each other. A magnified view of the 2PP-printed region is shown in the inset, with a detailed SEM image provided in Figure 4c. As can be observed, in TVAM-overprinted rectangular prisms, corners appear rounded mainly due to optical diffraction and dose accumulation effects, which blur sharp features [51]. In contrast, 2PP achieves sharp edges thanks to non-linear two-photon absorption and highly localized voxel-by-voxel printing.

In a second experiment, we focused the fs laser beam within the TVAM-overprinted part. As expected, the 2PP-printed bridge-like structure is not visible in the SEM images in Figure 4d since it is embedded within the TVAM printed part. However, the bridge-like 2PP structure is clearly observable under a phase contrast (PC) microscope, as shown in Figure 4e. This is because the PC microscope reveals variations in refractive index, which are not detectable in SEM, showing only surface morphology.

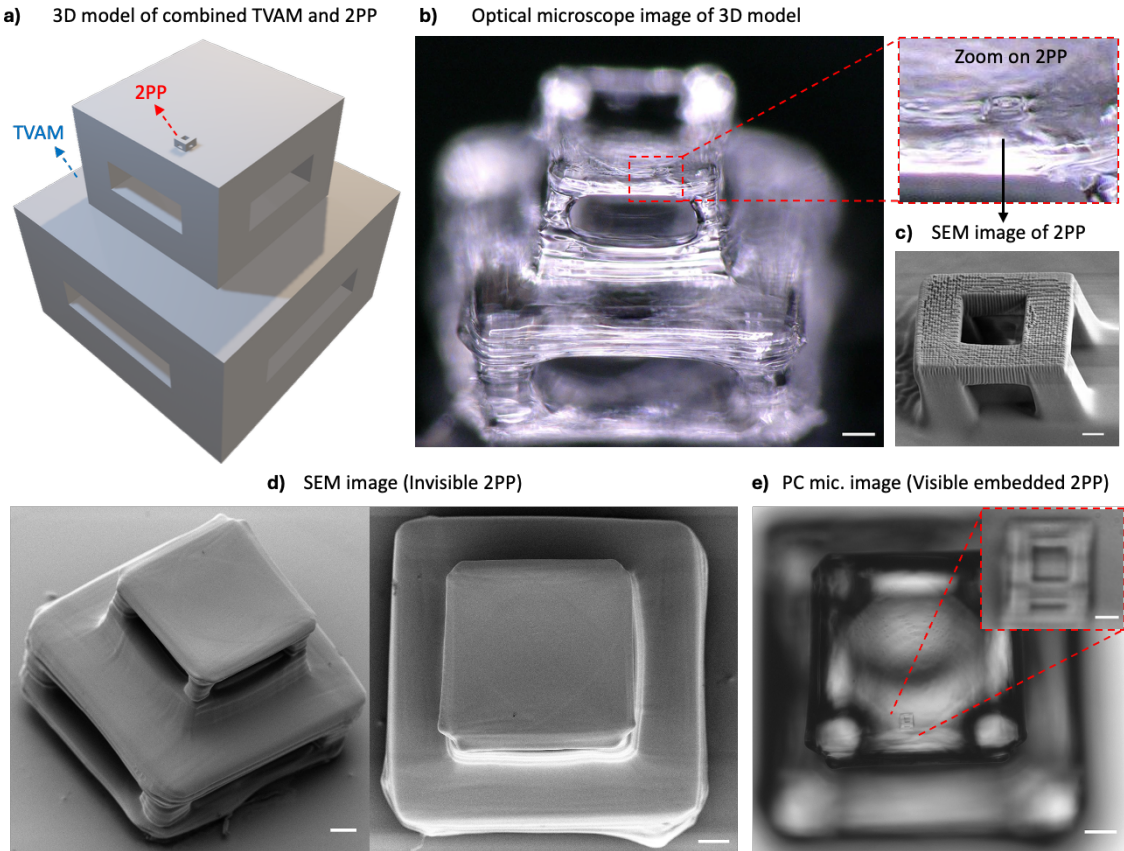


Figure 4. Two stacked rectangular prisms overprinted by TVAM, combined with a micrometer-scale bridge-like 2PP-printed structure. a) 3D CAD model for the combination of TVAM (two stacked rectangular prisms) and 2PP (bridge-like structure) printing. b) Digital microscope image of the printed model. The inset shows a magnified view of the bridge-like structure printed by 2PP. Scale bar is 100 μm . c) SEM image of the 2PP-printed bridge-like structure. Scale bar is 5 μm . d) SEM images of the printed final structure from a 40° tilt (left) and top view (right), showing TVAM-overprinted rectangular prisms, while the 2PP-printed bridge-like structure is not visible. The scale bars are 100 μm . e) PC microscope image of the same structure in which 2PP-printed part is observable. The inset shows a magnified view of the 2PP-printed bridge-like structure. The scale bars are 100 μm and 10 μm , respectively.

At present, the voxel rate in our proof-of-principle results were limited to 20 voxel/s by the frame rate of the LCOS SLM (60 fps) that controls the scanning laser beam and its driver program that requires three frames per voxel. The fabrication speed can be drastically improved using a resonant galvanometer scanning system and a high-speed optical modulator following recent reports [32]. For example, at a scanning rate of 8 kHz and 2.3 mm field of view (FOV) in our objective, a bidirectional scanning speed of 18.4 m/s could be achieved. Given the objective NA of 0.45, the smallest spot size for 2PP is approximately 0.86 μm , requiring a minimum modulation bandwidth of 22 MHz at the optical modulator, which can be readily fulfilled with commercial acousto-optic modulators. The voxel rate would then reach 2×10^7 voxel/s. The fabrication speed can be further improved with a faster version of resonant galvanometer (for example, 24 kHz) and more sensitive photoresin formulations [37,38].

4. Conclusion

We introduced a unified multiscale 3D printer proof of concept that integrates 2PP with single-photon TVAM, bridging the gap between high-precision and the exceptional speed and the volumetric throughput of the TVAM approach.

The volumetric nature of TVAM provides high throughput and rapid 3D fabrication by eliminating mechanical scanning and layer-by-layer stacking, both of which inherently limit the printing speed, while 2PP features the millimeter-scale TVAM-printed objects with nanometer-scale resolution. We combined these two complementary techniques within a single platform. Using the Dr.TVAM framework that models ray optical effects including refraction, absorption, and reflection, we accurately optimized light pattern for tomographic projections in TVAM and overprinted structures on a glass rod, enabling accessibility for subsequent 2PP on the surface or within the TVAM-printed structures.

We first experimentally demonstrated millimeter-scale TVAM-overprinted gears, on which, without changing the resin or applying post-processing, we subsequently printed a 270 nm resolution QR code by 2PP. The 3D printer also enabled printing multiple 2PP-printed structures along the rotational path of the rod, both using SLM scanning and through the direct fs laser exposure during the rod rotation, thereby increasing the accessible FOV and overall versatility of the multiscale 3D printer.

We further demonstrated the capability of our system by printing more complex structures. Millimeter-scale rectangular prisms with lateral through-holes were overprinted on the glass rod via TVAM and subsequently complemented with a bridge-like 2PP-printed structure, both on the surface and embedded inside the TVAM-printed prisms, achieving highly localized and precise features with sharp edges.

This unified multiscale 3D printer is particularly attractive for applications such as bioengineered scaffolds, microfluidic devices, and micro-optical components, enabling rapid, high-throughput fabrication of millimeter-scale structures with precisely localized sub-micrometer features.

CRediT authorship contribution statement

Buse Unlu: Writing - Original Draft, Performed experiments, Methodology, Software, Validation, Formal analysis, Investigation, Data Curation, Visualization, Project administration. **Felix Wechsler:** Writing - Review & Editing, Methodology, Software, Validation, Formal analysis, Investigation, Data Curation, Visualization. **Ye Pu:** Writing - Review & Editing, Methodology. **Christophe Moser:** Writing - Review & Editing, Conceptualization, Methodology, Supervision, Project administration, Funding acquisition.

Declaration of Competing Interest

Christophe Moser is a shareholder in Readily3D. All other authors declare no conflict of interest.

Data availability

The full configuration files and meshes for TVAM can be found at: <https://github.com/EPFL-LAPD/A-unified-multiscale-3D-printer-combining-single-photon-TVAM-and-Two-Photon-Polymerization>. Further data will be made available on request.

Acknowledgments

This project has received funding from the Swiss National Science Foundation 2000-1-240074 under grant number 10007068 - “Neural precision holographic volumetric additive manufacturing”.

References

- [1] C. Yu, J. Schimelman, P. Wang, K.L. Miller, X. Ma, S. You, J. Guan, B. Sun, W. Zhu, S. Chen, Photopolymerizable Biomaterials and Light-Based 3D Printing Strategies for Biomedical Applications, *Chem. Rev.* 120 (2020) 10695–10743. <https://doi.org/10.1021/acs.chemrev.9b00810>.
- [2] I. Gibson, D. Rosen, B. Stucker, *Additive Manufacturing Technologies: 3D Printing, Rapid Prototyping, and Direct Digital Manufacturing*, Springer New York, New York, NY, 2015. <https://doi.org/10.1007/978-1-4939-2113-3>.
- [3] M. Lee, R. Rizzo, F. Surman, M. Zenobi-Wong, Guiding Lights: Tissue Bioprinting Using Photoactivated Materials, *Chem. Rev.* 120 (2020) 10950–11027. <https://doi.org/10.1021/acs.chemrev.0c00077>.
- [4] B.E. Kelly, I. Bhattacharya, H. Heidari, M. Shusteff, C.M. Spadaccini, H.K. Taylor, Volumetric additive manufacturing via tomographic reconstruction, *Science* 363 (2019) 1075–1079. <https://doi.org/10.1126/science.aau7114>.
- [5] S.C. Ligon, B. Husár, H. Wutz, R. Holman, R. Liska, Strategies to Reduce Oxygen Inhibition in Photoinduced Polymerization, *Chem. Rev.* 114 (2014) 557–589. <https://doi.org/10.1021/cr3005197>.
- [6] P.N. Bernal, P. Delrot, D. Loterie, Y. Li, J. Malda, C. Moser, R. Levato, Volumetric Bioprinting of Complex Living-Tissue Constructs within Seconds, *Adv. Mater.* 31 (2019) 1904209. <https://doi.org/10.1002/adma.201904209>.
- [7] K.A. Robert, M.B. Thompson, Finer features for functional microdevices, *Nature* 412 (2001) 698–699. <https://doi.org/10.1038/35089135>.
- [8] V.F. Paz, M. Emons, K. Obata, A. Ovsianikov, S. Peterhansel, K. Frenner, C. Reinhardt, B. Chichkov, U. Morgner, W. Osten, Development of functional sub-100 nm structures with 3D two-photon polymerization technique and optical methods for characterization, *J. Laser Appl.* 24 (2012) 042004. <https://doi.org/10.2351/1.4712151>.
- [9] D. Loterie, P. Delrot, C. Moser, High-resolution tomographic volumetric additive manufacturing, *Nat. Commun.* 11 (2020) 852. <https://doi.org/10.1038/s41467-020-14630-4>.
- [10] T.H. Weisgraber, M.P. De Beer, S. Huang, J.J. Karnes, C.C. Cook, M. Shusteff, Virtual Volumetric Additive Manufacturing (VirtualVAM), *Adv. Mater. Technol.* 8 (2023) 2301054. <https://doi.org/10.1002/admt.202301054>.
- [11] M.I. Álvarez-Castaño, A.G. Madsen, J. Madrid-Wolff, V. Sgarminato, A. Boniface, J. Glückstad, C. Moser, Holographic tomographic volumetric additive manufacturing, *Nat. Commun.* 16 (2025) 1551. <https://doi.org/10.1038/s41467-025-56852-4>.
- [12] Y. Zhang, H. De Haan, K. Houlahan, K.L. Sampson, D. Webber, A. Orth, T. Lacelle, L. Gaburici, R. Lam, B. Deore, C. Paquet, Impact of oxygen inhibition on (meth)acrylate photopolymerization in tomographic volumetric printing, *Addit. Manuf.* 109 (2025) 104844. <https://doi.org/10.1016/j.addma.2025.104844>.

[13] J.T. Toombs, M. Lutz, C.C. Cook, S. Jenne, C.C. Li, B.E. Rapp, F. Kotz-Helmer, H.K. Taylor, Volumetric additive manufacturing of silica glass with microscale computed axial lithography, *Science* 376 (2022) 308–312. <https://doi.org/10.1126/science.abm6459>.

[14] F. Natterer, Inversion of the attenuated Radon transform, *Inverse Probl.* 17 (2001) 113–119. <https://doi.org/10.1088/0266-5611/17/1/309>.

[15] D. Webber, Y. Zhang, M. Picard, J. Boisvert, C. Paquet, A. Orth, Versatile volumetric additive manufacturing with 3D ray tracing, *Opt. Express* 31 (2023) 5531. <https://doi.org/10.1364/OE.481318>.

[16] B. Nicolet, F. Wechsler, J. Madrid-Wolff, C. Moser, W. Jakob, Inverse Rendering for Tomographic Volumetric Additive Manufacturing, *ACM Trans. Graph.* 43 (2024) 1–17. <https://doi.org/10.1145/3687924>.

[17] F. Wechsler, C. Gigli, J. Madrid-Wolff, C. Moser, Wave optical model for tomographic volumetric additive manufacturing, *Opt. Express* 32 (2024) 14705. <https://doi.org/10.1364/OE.521322>.

[18] C.M. Rackson, K.M. Champley, J.T. Toombs, E.J. Fong, V. Bansal, H.K. Taylor, M. Shusteff, R.R. McLeod, Object-space optimization of tomographic reconstructions for additive manufacturing, *Addit. Manuf.* 48 (2021) 102367. <https://doi.org/10.1016/j.addma.2021.102367>.

[19] I. Bhattacharya, J. Toombs, H. Taylor, High fidelity volumetric additive manufacturing, *Addit. Manuf.* 47 (2021) 102299. <https://doi.org/10.1016/j.addma.2021.102299>.

[20] F. Wechsler, C. Gigli, J. Madrid-Wolff, C. Moser, SwissVAMyKnife.jl: An open-source package for tomographic volumetric additive manufacturing, *EPJ Web Conf.* 309 (2024) 03024. <https://doi.org/10.1051/epjconf/202430903024>.

[21] C.C. Li, J.T. Toombs, H.K. Taylor, T.J. Wallin, Generalized projection optimization model for tomographic volumetric additive manufacturing, in: G. Von Freymann, E. Blasco, D. Chanda (Eds.), *Adv. Fabr. Technol. MicroNano Opt. Photonics XVII*, SPIE, San Francisco, United States, 2024: p. 35. <https://doi.org/10.1117/12.3008459>.

[22] J. Madrid-Wolff, J. Toombs, R. Rizzo, P.N. Bernal, D. Porcincula, R. Walton, B. Wang, F. Kotz-Helmer, Y. Yang, D. Kaplan, Y.S. Zhang, M. Zenobi-Wong, R.R. McLeod, B. Rapp, J. Schwartz, M. Shusteff, H. Talyor, R. Levato, C. Moser, A review of materials used in tomographic volumetric additive manufacturing, *MRS Commun.* 13 (2023) 764–785. <https://doi.org/10.1557/s43579-023-00447-x>.

[23] F. Wechsler, V. Sgarminato, R. Rizzo, B. Nicolet, W. Jakob, C. Moser, Overprinting with Tomographic Volumetric Additive Manufacturing, (2025). <https://doi.org/10.48550/arXiv.2507.13842>.

[24] S. Florczak, G. Größbacher, D. Ribetti, A. Longoni, M. Gueye, E. Grandidier, J. Malda, R. Levato, Adaptive and Context-Aware Volumetric Printing, (n.d.).

[25] E. Papagiakoumou, E. Ronzitti, V. Emiliani, Scanless two-photon excitation with temporal focusing, *Nat. Methods* 17 (2020) 571–581. <https://doi.org/10.1038/s41592-020-0795-y>.

[26] V. Harinarayana, Y.C. Shin, Two-photon lithography for three-dimensional fabrication in micro/nanoscale regime: A comprehensive review, *Opt. Laser Technol.* 142 (2021) 107180. <https://doi.org/10.1016/j.optlastec.2021.107180>.

[27] M. Göppert-Mayer, Elementary processes with two quantum transitions, *Ann. Phys.* 521 (2009) 466–479. <https://doi.org/10.1002/andp.200952107-804>.

[28] I. Boudene, Y. Bougdid, Two-photon polymerization-assisted 3D laser nanoprinting: from fundamentals to modern applications, *J. Mater. Chem. C* 13 (2025) 18597–18630. <https://doi.org/10.1039/D5TC02037A>.

[29] L. Zheng, K. Kurselis, A. El-Tamer, U. Hinze, C. Reinhardt, L. Overmeyer, B. Chichkov, Nanofabrication of High-Resolution Periodic Structures with a Gap Size Below 100 nm by Two-Photon Polymerization, *Nanoscale Res. Lett.* 14 (2019) 134. <https://doi.org/10.1186/s11671-019-2955-5>.

[30] F. Burmeister, S. Steenhusen, R. Houbertz, U.D. Zeitner, S. Nolte, A. Tünnermann, Materials and technologies for fabrication of three-dimensional microstructures with sub-100 nm feature sizes by two-photon polymerization, *J. Laser Appl.* 24 (2012) 042014. <https://doi.org/10.2351/1.4730807>.

[31] W. Cao, W. Yu, Z. Xiao, D. Qi, Z. Wang, W. Xin, Y. Wu, Y. Deng, H. Zheng, Water repellence of biomimetic structures fabricated via femtosecond laser direct writing, *J. Manuf. Process.* 102 (2023) 644–653. <https://doi.org/10.1016/j.jmapro.2023.07.076>.

[32] S. Binder, F. Chalupa-Gantner, H.W. Yoo, T. Zandrin, A. Ovsianikov, Two-photon polymerization system based on a resonant scanner for high-throughput production of tissue engineering microscaffolds, *Addit. Manuf.* 97 (2025) 104601. <https://doi.org/10.1016/j.addma.2024.104601>.

[33] L. Zhang, C. Wang, C. Zhang, Y. Xue, Z. Ye, L. Xu, Y. Hu, J. Li, J. Chu, D. Wu, High-Throughput Two-Photon 3D Printing Enabled by Holographic Multi-Foci High-Speed Scanning, *Nano Lett.* 24 (2024) 2671–2679. <https://doi.org/10.1021/acs.nanolett.4c00505>.

[34] C. Maibohm, O.F. Silvestre, J. Borme, M. Sinou, K. Heggarty, J.B. Nieder, Multi-beam two-photon polymerization for fast large area 3D periodic structure fabrication for bioapplications, *Sci. Rep.* 10 (2020) 8740. <https://doi.org/10.1038/s41598-020-64955-9>.

[35] V. Hahn, P. Kiefer, T. Frenzel, J. Qu, E. Blasco, C. Barner-Kowollik, M. Wegener, Rapid Assembly of Small Materials Building Blocks (Voxels) into Large Functional 3D Metamaterials, *Adv. Funct. Mater.* 30 (2020) 1907795. <https://doi.org/10.1002/adfm.201907795>.

[36] Q. Geng, D. Wang, P. Chen, S.-C. Chen, Ultrafast multi-focus 3-D nano-fabrication based on two-photon polymerization, *Nat. Commun.* 10 (2019) 2179. <https://doi.org/10.1038/s41467-019-10249-2>.

[37] Z. Ma, T. Li, X. Dai, X. Shen, X. Wang, H. Fu, X. Xia, Q. Zhu, Y. Zhu, Z. Yu, C. Cao, S. You, C. Kuang, Highly Sensitive Cationic Photoresist for High-Throughput Two-Photon Nanofabrication, *Adv. Funct. Mater.* 34 (2024) 2409859. <https://doi.org/10.1002/adfm.202409859>.

[38] T. Liu, P. Tao, X. Wang, H. Wang, M. He, Q. Wang, H. Cui, J. Wang, Y. Tang, J. Tang, N. Huang, C. Kuang, H. Xu, X. He, Ultrahigh-printing-speed photoresists for additive manufacturing, *Nat. Nanotechnol.* 19 (2024) 51–57. <https://doi.org/10.1038/s41565-023-01517-w>.

[39] A. Grabulosa, J. Moughames, X. Porte, D. Brunner, Combining one and two photon polymerization for accelerated high performance (3 + 1)D photonic integration, *Nanophotonics* 11 (2022) 1591–1601. <https://doi.org/10.1515/nanoph-2021-0733>.

[40] A.I. Akash, J.E. Johnson, F.C. Arentz, X. Xu, Two-color 3D printing for reduction in femtosecond laser printing power, *Opt. Express* 32 (2024) 25892. <https://doi.org/10.1364/OE.525826>.

[41] B. Unlu, M.I. Álvarez-Castaño, A. Boniface, Y. Pu, C. Moser, Single-photon-assisted two-photon polymerization, *Addit. Manuf.* 94 (2024) 104455. <https://doi.org/10.1016/j.addma.2024.104455>.

[42] M. Halendy, S. Ertman, Q. Huang, X. Dong, P.P. Shum, T.R. Woliński, Dual-Refractive-Index Photonic Crystal Waveguides Fabricated by Combining Two-Photon Polymerization 3D Nanoprinting with Dose-Modified One-Photon Polymerization, *Adv. Opt. Mater.* 13 (2025) 2500500. <https://doi.org/10.1002/adom.202500500>.

[43] M. Malinauskas, A. Žukauskas, S. Hasegawa, Y. Hayasaki, V. Mizeikis, R. Buividas, S. Juodkazis, Ultrafast laser processing of materials: from science to industry, *Light Sci. Appl.* 5 (2016) e16133–e16133. <https://doi.org/10.1038/lsa.2016.133>.

[44] M. Schmid, D. Ludescher, H. Giessen, Optical properties of photoresists for femtosecond 3D printing: refractive index, extinction, luminescence-dose dependence, aging, heat treatment and comparison between 1-photon and 2-photon exposure, *Opt. Mater. Express* 9 (2019) 4564. <https://doi.org/10.1364/OME.9.004564>.

[45] Y. Li, S. Park, M. McLamb, M. Lata, S. Schöche, D. Childers, I.D. Aggarwal, M.K. Poutous, G. Boreman, T. Hofmann, UV to NIR optical properties of IP-Dip, IP-L, and IP-S after two-photon polymerization determined by spectroscopic ellipsometry, *Opt. Mater. Express* 9 (2019) 4318. <https://doi.org/10.1364/OME.9.004318>.

[46] T. Baldacchini, C.N. LaFratta, R.A. Farrer, M.C. Teich, B.E.A. Saleh, M.J. Naughton, J.T. Fourkas, Acrylic-based resin with favorable properties for three-dimensional two-photon polymerization, *J. Appl. Phys.* 95 (2004) 6072–6076. <https://doi.org/10.1063/1.1728296>.

[47] C.R. Mendonca, D.S. Correa, T. Baldacchini, P. Tayalia, E. Mazur, Two-photon absorption spectrum of the photoinitiator Lucirin TPO-L, *Appl. Phys. A* 90 (2008) 633–636. <https://doi.org/10.1007/s00339-007-4367-0>.

[48] G. Ummethala, A. Jaiswal, R.P. Chaudhary, S. Hawal, S. Saxena, S. Shukla, Localized polymerization using single photon photoinitiators in two-photon process for fabricating subwavelength structures, *Polymer* 117 (2017) 364–369. <https://doi.org/10.1016/j.polymer.2017.04.039>.

[49] N. Uppal, P.S. Shiakolas, Process Sensitivity Analysis and Resolution Prediction for the Two Photon Polymerization of Micro/Nano Structures, *J. Manuf. Sci. Eng.* 131 (2009) 051018. <https://doi.org/10.1115/1.4000097>.

[50] P. Skurowski, K. Nurzyńska, M. Pawlyta, K.A. Cyran, Performance of QR Code Detectors near Nyquist Limits, *Sensors* 22 (2022) 7230. <https://doi.org/10.3390/s22197230>.

[51] A. Orth, D. Webber, Y. Zhang, K.L. Sampson, H.W. De Haan, T. Lacelle, R. Lam, D. Solis, S. Dayanandan, T. Waddell, T. Lewis, H.K. Taylor, J. Boisvert, C. Paquet, Deconvolution volumetric additive manufacturing, *Nat. Commun.* 14 (2023) 4412. <https://doi.org/10.1038/s41467-023-39886-4>.

A unified multiscale 3D printer combining single-photon Tomographic Volumetric Additive Manufacturing and Two-Photon Polymerization:

Supplementary Materials

Buse Unlu^{1,*}, Felix Wechsler¹, Ye Pu¹, Christophe Moser¹

¹Laboratory of Applied Photonics Devices, School of Engineering, Ecole Polytechnique Fédérale de Lausanne, CH-1015, Lausanne, Switzerland

Corresponding author: buse.unlu@epfl.ch

Experimental setup for tomographic volumetric additive manufacturing

The optical setup used for tomographic volumetric additive manufacturing (TVAM) is illustrated in Figure S1. A continuous-wave (CW) laser diode at 405 nm (HL40033G, Ushio) is coupled into a square-core multimode fiber (70 μ m x 70 μ m core size, NA = 0.22, WF 70x70/115/200/400N, CeramOptec) by means of a collimator (L1, f = 4.02 mm, NA = 0.6, F671APC-405, Thorlabs) and an aspheric lens (L2, f = 15.3 mm, NA = 0.16, C260TMD-A, Thorlabs), respectively. The light output from the fiber is collimated using an achromatic doublet (L3, f = 100 mm, AC254-100-A-ML, Thorlabs) and projected onto the aperture of a Digital Micromirror Device (DMD, V-7000 VIS, Vialux). The light patterns generated by the DMD are directed through mirrors (M1 and M2) and demagnified by 2 via a lens pair of achromatic doublets, L4 (f = 300 mm, AC508-300-A-ML, Thorlabs) and L5 (f = 150 mm, AC254-150-A-ML, Thorlabs). An iris placed in the Fourier plane between L4 and L5 acts as a spatial filter blocking high diffraction orders from the DMD and constraining the angular divergence of the beam.

A quartz glass vial (refractive index 1.4696, inner diameter 4.30 mm) is mounted on a motorized rotary stage (X-RSW60C, Zaber), which is then placed on top of a one-axis motorized translation stage (PT1/M-Z9, Thorlabs) providing z-axis motion. This assembly is mounted on a two-axis linear translation stage (XYT1/M, Thorlabs) for xy-axis motion and is positioned at the center of the DMD image plane.

The patterns and the printing process are monitored by a camera (acA2040-55um, Basler) using two achromatic doublets, L6 and L7 (AC254-075-A-ML, Thorlabs), and illuminated by a laser diode at 650 nm (VLM-650-01 LPT, Quarton Inc.).

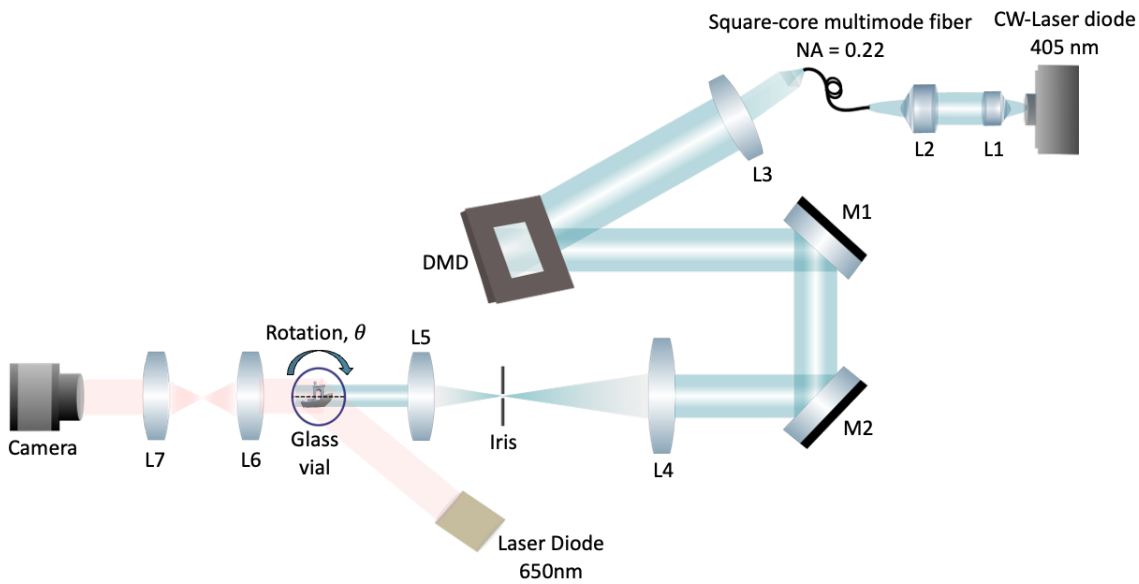


Figure S1. Illustration of the experimental setup for TVAM.

Experimental setup for two-photon polymerization

The two-photon polymerization setup used in this work follows the configuration described in detail in the Supplementary Materials (Section S1 and S5) of our previous publication [1], with modifications to the printing region in Figure S2. We currently use a double-sided-cut quartz glass vial (refractive index 1.4696, inner diameter 4.30 mm) to place the photoresin. In order to satisfy the requirements of the objective lens OBL (Zeiss A-Plan 20 \times , NA = 0.45), a 170 μ m-thick coverslip is glued to the bottom of the glass vial using an optical adhesive. A glass rod (made of borosilicate glass 3.3, ends circular cut, L = 100 \pm 0.5, Diameter = 1 \pm 0.05 mm, Hilgenberg GmbH) is inserted into the resin and serves as the printing platform. Both the glass vial and the glass rod are mounted on separate motorized rotary stages (X-RSW60C, Zaber) as required for TVAM (not for 2PP). Each rotary stage is placed on top of a one-axis motorized translation stage (PT1/M-Z9, Thorlabs) providing z-axis motion, and these assemblies are then mounted on a two-axis linear translation stage (XYT1/M, Thorlabs) for xy-axis motion.

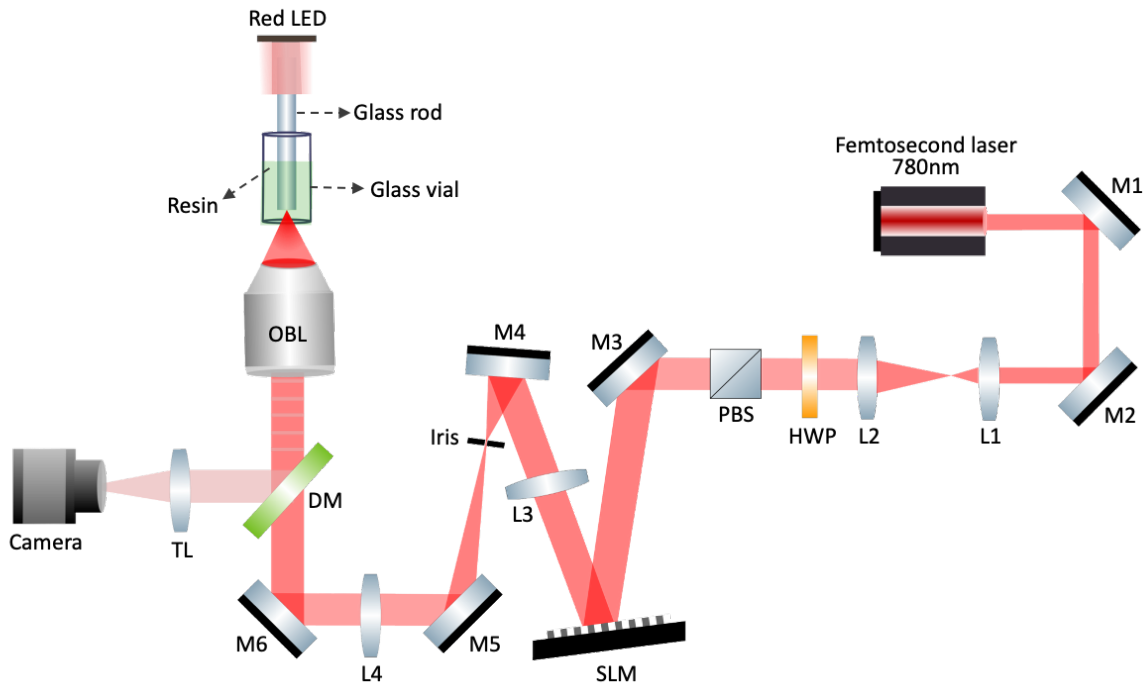


Figure S2. Illustration of the experimental setup for 2PP.

Printing region of multiscale 3D Printer combining TVAM and 2PP

A real photograph of the printing region taken from the setup where the TVAM and 2PP systems are combined is shown in Figure S3. The TVAM system (L5, in Figure S1) is positioned orthogonally to the IR fs laser beam (OBJ, in Figure S2). A glass rod is dipped into the resin vial where both are mounted on rotary stages.

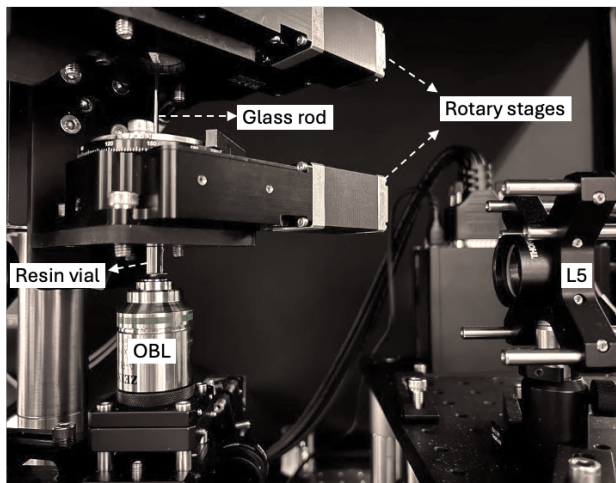


Figure S3. Real photograph of the printing region in the combined TVAM and 2PP setup.

Spot diagram analysis of the tomographic volumetric additive manufacturing system

Ray-tracing simulations were performed to check the aberration of the beam spot in the printing region of the TVAM using Zemax OpticStudio. We obtained the spot diagrams that

depict the ray-intersection distribution on the image plane for three field points: on-axis (center focus) and at 10 mm and 14 mm off-axis, as shown in Figure S4, indicated by OBJ: 0.00, 10.00, and 14.00 mm. The results indicate a root-mean-square (RMS) point-spread-function (PSF) diameter of approximately 6.8 μm . Aberrations introduced by the glass vial and the photoresin were not included in these optical simulations, which are corrected in TVAM optimizations.

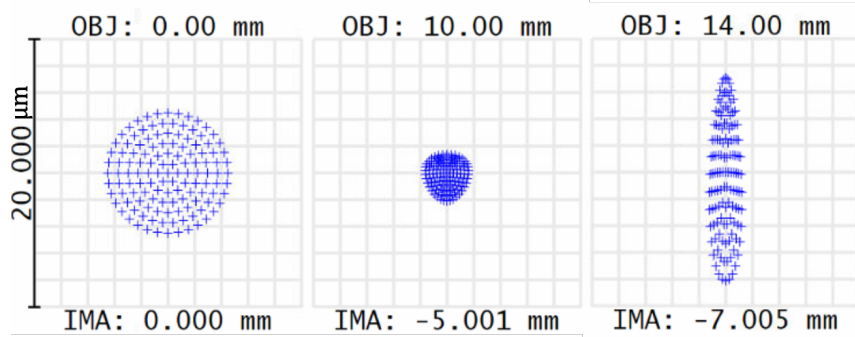


Figure S4. Spot diagrams from ray tracing simulations performed by Zemax OpticStudio: on-axis and off-axis at 10 mm and 14 mm, respectively.

Energy dose calculation for TVAM

Calculating the absorbed dose of object voxels in TVAM is not a simple equation. Since in TVAM each pattern pixel projects a different intensity and since we intentionally craft the patterns to have a spatially varying absorbed 3D dose, the physical dose is heavily dependent on object properties but also resin parameters and optimization parameters (such as the thresholds and the weight of the sparsity term).

With our framework Dr.TVAM, as a first step we can calculate the energy efficiency of the patterns with

$$\text{Pattern Energy Efficiency} = \frac{\sum_{p \in \text{patterns}} p}{\max(\text{patterns})} \frac{1}{N_{pixels}}$$

We need to divide each pattern value by the maximum value of all pattern pixels, since the DMD in experiments normalizes all patterns with respect to the brightest value. The energy efficiency describes the ratio of projected energy and theoretically available energy.

From Dr.TVAM we can then numerically calculate how much of this projected energy is absorbed in the object voxels, how much is absorbed in the void voxels, and how much is transmitted through the vial.

Dr.TVAM exports a unitless energy per volume value with the final patterns. This value has to be multiplied by the measured power of the laser (if all DMD pixels are fully turned on) and the total printing time. The result is an energy dose in Joule per cubic meter.

For our two experiments (gear and rectangular prisms), the values are, respectively,

$$103650.523 \frac{1}{\text{m}^3} \times 36.4 \text{ mW} \times 12 \text{ s} = 45.3 \frac{\text{mJ}}{\text{cm}^3}$$

and

$$60606.586 \frac{1}{m^3} \times 70.5 \text{ mW} \times 12 \text{ s} = 51.3 \frac{mJ}{cm^3}$$

This value indicates the energy required to cause polymerization. Note that this energy threshold is also dependent on parameters such as concentration and type of photoinitiator, the resin, and the concentration of inhibitors. Since we use the same resin for both experiments, we also expect to have roughly the same energy threshold.

Photosensitive resin used for fabrication

A photocurable resin is formulated by mixing diurethane dimethacrylate (DUDMA) and poly(ethylene glycol) diacrylate (PEGDA, average Mn 700) in a 4:1 weight ratio, with 1.35 wt.% ethyl-2,4,6trimethylbenzoylphenylphosphinate (TPO-L) as the photoinitiator, which absorbs both single- and two-photon excitation [1–5]. The refractive index of the resin is measured as 1.4827 at 405 nm via a refractometer (AR200, Reichert). To determine the absorbance of the resin, we prepared samples with lower TPO-L concentrations (0.11, 0.15, 0.2, 0.27, and 0.3 wt.%), as the 1.35 wt.% concentration exceeds the device's measurement capabilities, and measured the absorbance at 405 nm in Figure S5. Using these data, we applied a linear fit to extrapolate the absorbance of the resin formulated with 1.35 wt.% TPO-L, which was calculated to be 4.695, providing the extinction coefficient of 1.081 mm^{-1} .

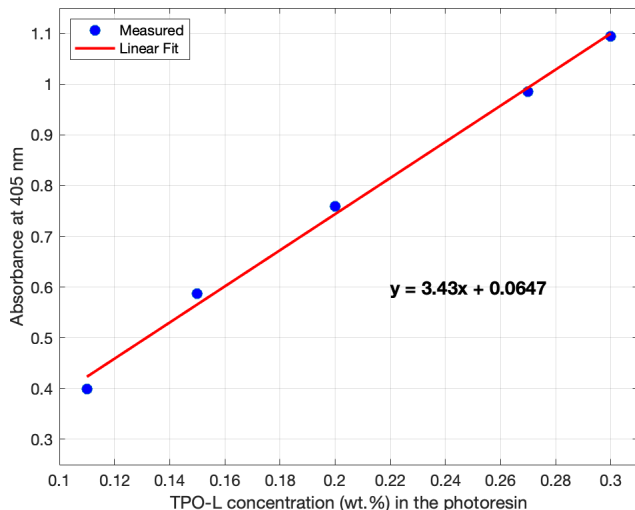


Figure S5. Absorbance values of the resin composed of DUDMA and PEGDA (4:1 weight ratio) with TPO-L photoinitiator concentrations of 0.11, 0.15, 0.2, 0.27, and 0.3 wt.%. A linear fit is applied to obtain the equation for calculating the 1.35 wt.% TPO-L absorbance.

Fluid dynamics of photoresin under rotational motion

When we printed a gear with only one full rotation of the glass vial before illuminating the DMD patterns, the gear teeth were not straight but instead curved in one direction, as shown in Figure S6a. This effect arose from a mismatch between the rotational speed of the vial and the liquid resin. At the beginning of the rotation, the bulk of the liquid remains still due to the inertia. Only the liquid layer immediately next to the wall of the container moves with the container due to the nonslip condition, forming a radial velocity gradient which results in a

shear stress in the liquid. The rest of the liquid is then driven by the shearing force, forming a typical shear-driven flow system [6]. Depending on the viscosity of the liquid, there is a time delay for the entire liquid bulk to rotate at the same speed before which the existence of a shear-driven flow in the liquid bulk causes printing distortion. When we rotated the vial three full rotations before illuminating the patterns, the resulting teeth were straight (in Figure S6b), as this allowed the resin to reach a uniform rotational speed throughout.

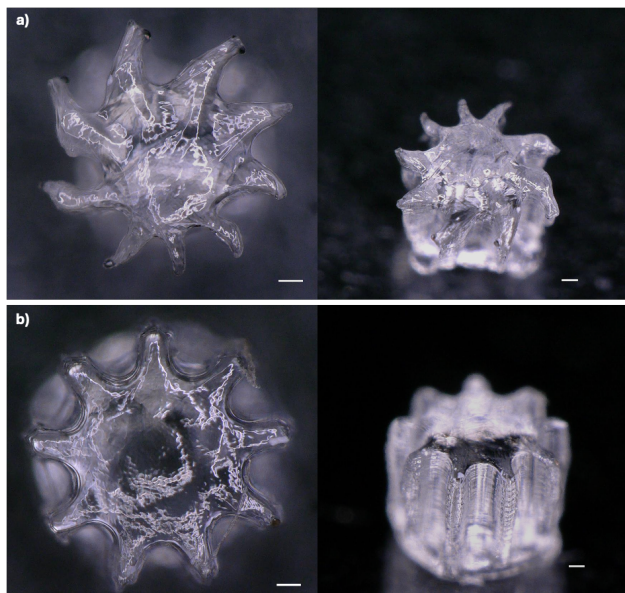


Figure S6. Digital microscope image of the TVAM-overprinted gear (top and side views, respectively) with a) one and b) three full rotations of the glass vial prior to DMD pattern illumination. The scale bars are 100 μm .

References

- [1] B. Unlu, M.I. Álvarez-Castaño, A. Boniface, Y. Pu, C. Moser, Single-photon-assisted two-photon polymerization, *Addit. Manuf.* 94 (2024) 104455. <https://doi.org/10.1016/j.addma.2024.104455>.
- [2] T. Baldacchini, C.N. LaFratta, R.A. Farrer, M.C. Teich, B.E.A. Saleh, M.J. Naughton, J.T. Fourkas, Acrylic-based resin with favorable properties for three-dimensional two-photon polymerization, *J. Appl. Phys.* 95 (2004) 6072–6076. <https://doi.org/10.1063/1.1728296>.
- [3] C.R. Mendonca, D.S. Correa, T. Baldacchini, P. Tayalia, E. Mazur, Two-photon absorption spectrum of the photoinitiator Lucirin TPO-L, *Appl. Phys. A* 90 (2008) 633–636. <https://doi.org/10.1007/s00339-007-4367-0>.
- [4] G. Ummethala, A. Jaiswal, R.P. Chaudhary, S. Hawal, S. Saxena, S. Shukla, Localized polymerization using single photon photoinitiators in two-photon process for fabricating subwavelength structures, *Polymer* 117 (2017) 364–369. <https://doi.org/10.1016/j.polymer.2017.04.039>.
- [5] N. Uppal, P.S. Shiakolas, Process Sensitivity Analysis and Resolution Prediction for the Two Photon Polymerization of Micro/Nano Structures, *J. Manuf. Sci. Eng.* 131 (2009) 051018. <https://doi.org/10.1115/1.4000097>.
- [6] Y.A. Çengel, J.M. Cimbala, *Fluid mechanics: fundamentals and applications*, 3. ed, McGraw-Hill, New York, NY, 2014.